

CONSTRAINING GLOBULAR CLUSTER AGE UNCERTAINTIES USING THE IR COLOR-MAGNITUDE DIAGRAM¹MATTEO CORRENTI², MARIO GENNARO², JASON S. KALIRAI^{2,3}, THOMAS M. BROWN², AND ANNALISA CALAMIDA²*Draft version March 4, 2024*

ABSTRACT

Globular Clusters (GCs) in the Milky Way are the primary laboratories for establishing the ages of the oldest stellar populations and for measuring the color-magnitude relation of stars. In infrared (IR) color-magnitude diagrams (CMDs), the stellar main sequence (MS) exhibits a “kink”, due to opacity effects in M dwarfs, such that lower mass and cooler dwarfs become bluer in the IR color baseline. This diagnostic offers a new opportunity to model GC CMDs and to reduce uncertainties on cluster properties (e.g., their derived ages). In this context, we analyzed Hubble Space Telescope Wide Field Camera 3 IR archival observations of four GCs – 47 Tuc, M4, NGC 2808, and NGC 6752 – for which the data are deep enough to fully sample the low-mass MS, reaching at least $\simeq 2$ mag below the “kink”. We derived the fiducial lines for each cluster and compared them with a grid of isochrones over a large range of parameter space, allowing age, metallicity, distance, and reddening to vary within reasonable selected ranges. The derived ages for the four clusters are respectively 11.6, 11.5, 11.2, and 12.1 Gyr and their random uncertainties are $\sigma \sim 0.7 - 1.1$ Gyr. Our results suggest that the near-IR MS “kink”, combined with the MS turn-off, provides a valuable tool to measure GC ages and offers a promising opportunity to push the absolute age of GCs to sub-Gyr accuracy with the next generation IR telescopes such as the James Webb Space Telescope and the Wide-Field Infrared Survey Telescope.

Subject headings: galaxies: star clusters — globular clusters: general

1. INTRODUCTION

Globular Clusters (GCs) are among the oldest objects in the Universe and accompany most major star formation episodes in galaxies (e.g. Brodie & Strader 2006). The *absolute* age determination of the population represents one of the most reliable measures of when baryonic structure formation occurred in the Universe (Spergel et al. 2003) and provides robust constraints on the physics adopted in stellar evolutionary models (Salaris & Weiss 1998; Cassisi et al. 1999; VandenBerg et al. 2008; Dotter et al. 2008). The *relative* age difference between clusters associated with distinct structural components establishes the formation and assembly timescales of these parent populations (e.g., the bulge, halo, and substructure).

Modern derivations of star cluster ages have primarily involved reproducing visible-light color-magnitude diagrams (CMDs) with stellar evolutionary models. However, estimates of absolute GC ages are hampered by uncertainties in other fundamental parameters: in addition to accounting for systematic uncertainties due to different assumptions in stellar models ($\sigma = 0.4$ Gyr – Chaboyer & Krauss 2002; Valle et al. 2013a,b) and the cluster metallicity ($\sigma = 0.5$ Gyr for a 0.2 dex error – Dotter et al. 2008), the largest uncertainty impacting this technique comes from simultaneously “fitting” the age at a given distance and reddening ($\sigma = 1.5 - 2$ Gyr – Chaboyer 2008). On visible CMDs, the latter quantities are estimated by aligning the luminosity of the horizontal branch and the slope of the unevolved main sequence (MS) to the observations (e.g., Iben & Renzini 1984).

Different methods have been proposed to overcome some of these problems: the use of a different clock (white

dwarf cooling sequence, Hansen et al. 2013, and references therein), different photometric systems (Strömgren bands, Grundahl et al. 1998), or different diagnostics (luminosity function, Zoccali et al. 2000; Richer et al. 2008).

Bono et al. (2010) introduced a new tool to measure accurate star cluster parameters, based on high-precision infrared (IR) CMDs. In fact, the MS in a pure IR CMD exhibits a “kink” (hereafter we refer to it simply as kink) at $\sim 0.5 M_{\odot}$, i.e. turns towards bluer colors (Pulone et al. 1998, 1999; Zoccali et al. 2000; Calamida et al. 2009; Sarajedini et al. 2009; Kalirai et al. 2012; Milone et al. 2012, 2014; Monelli et al. 2015). This feature arises from a redistribution of the emerging stellar flux due to a change in opacity caused by the collision-induced absorption of H_2 (Linsky 1969; Saumon et al. 1994, and references therein). The theoretical predictions of temperature and luminosity of the kink are minimally affected by uncertainties in the treatment of convection (i.e., by mixing length theory calibration), as the convective motions are nearly adiabatic at these masses (Saumon & Marley 2008). The luminosity of the kink and the shape of the bending are dependent on metallicity, but are independent of age beyond ~ 1 Gyr. Therefore, the degeneracy between these two parameters can be partially broken. Equally as important, the shape of the color-magnitude relation in the IR CMD, in particular its inversion at magnitude fainter than the kink, provides a new opportunity to simultaneously constrain the distance and reddening accurately. Therefore, this new diagnostic provides a large lever arm to decrease the uncertainties involved in deriving GC age estimates.

To test the power of this feature to establish accurate GC properties, we searched the MAST STScI-archive for public Wide Field Camera 3 (WFC3) IR data sampling a set of Milky Way GCs. There are a dozen clusters for which such data are available, but, only for four GCs, namely 47 Tuc, M4, NGC 2808, and NGC 6752, the data are deep enough to reach $\simeq 2$ mag below the kink. This depth is required to fully sample the bending of the MS at low masses. The four GCs provide a good sample to test the predictive power of the MS kink

¹ Based on observations with the NASA/ESA *Hubble Space Telescope*, obtained at the Space Telescope Science Institute, which is operated by the Association of Universities for Research in Astronomy, Inc., under NASA contract NAS5-26555

² Space Telescope Science Institute, 3700 San Martin Drive, Baltimore, MD 21218, USA; correnti, gennaro, jkalirai, tbrown, calamida@stsci.edu

³ Center for Astrophysical Science, John Hopkins University, Baltimore, MD 21218, USA

Table 1
Description of the datasets

Cluster (1)	Exposure Time (2)	Filter (3)	Program (4)	PI (5)
47 Tuc ^a	91.8 ks 185.6 ks	F110W F160W	11677	H. Richer
M 4	5.2 ks 10.4 ks	F110W F160W	12602	A. Dieball
NGC 2808	3 × 1.4 ks 3 × 1.7 ks	F110W F160W	11665	T. M. Brown
NGC 6752	0.7 ks 0.7 ks	F110W F160W	11664	T. M. Brown

Note. — Columns (1): Name of the clusters. (2): Total exposure time (kiloseconds). (3): Filter. (4): Program identification number. (5): Principal Investigator.

^aWe reported the combined integration time of the *Swath* and *Stare* fields. For a detailed description of 47 Tuc observational strategy we refer the reader to Kalirai et al. (2012).

thoroughly, as they span a significant range of metallicity ($[\text{Fe}/\text{H}] \simeq -0.7$ – -1.5 dex), distance ($d_{\odot} \simeq 2.1$ – 9.6 kpc) and reddening ($E(B-V) \simeq 0.04$ – 0.39 dex).

Using an ad-hoc fitting method, we derived a fiducial line in the CMD for each GC. These fiducial lines represent the loci where we expect the single stars (i.e., excluding binaries and higher multiples) of the cluster to lie if they were observed without errors. We compared these fiducials with a grid of isochrones and derived the joint posterior probability density function (PDF) for the four parameters, age, metallicity, distance and reddening. This, in turn, allowed us to estimate the best fitting parameters, quantify the correlations among them and derive the uncertainties of the individual parameters. In this paper, we focus on the derived GC ages, by marginalizing the joint PDF over the remaining three parameters.

Our analysis demonstrates the importance of the near-IR MS kink as an age diagnostic, and illustrates how this feature can provide the first opportunity to push the absolute ages of GCs to sub-Gyr precision.

The remainder of the paper is organized as follows: we present the data set and reduction in Section 2 and the CMDs of the four GCs in Section 3. We also describe the method adopted to measure the fiducial lines for each of the GCs. In Section 4 we derive the best-fit isochrones and the probability distribution functions, thereby obtaining an estimate of the age and uncertainty for each GC. In Section 5 we discuss the results from our study.

2. SAMPLE AND DATA REDUCTION

Our sample consists of four clusters: 47 Tuc (GO-11677, PI: H. Richer), M 4 (GO-12602, PI: A. Dieball), NGC 2808 (GO-11665, PI: T. M. Brown), and NGC 6752 (GO-11664, PI: T. M. Brown). With the exception of 47 Tuc, for which the photometry has been derived in Kalirai et al. (2012), we downloaded from the MAST STScI-archive the images for the other three clusters. A description of these datasets is provided in Table 1.

To reduce the images of M 4, NGC 2808 and NGC 6752 we followed the same method adopted for 47 Tuc, described in detail in Kalirai et al. (2012). Briefly, we started from the *flt* files provided by the HST pipeline, which constitute the bias-corrected, dark-subtracted and flat-fielded images. We generated distortion-free images using MultiDrizzle (Fruchter & Hook 1997) and we calculated the transformation between the individual drizzled images in each filter, linking them to a reference frame (i.e., the first exposure). Through these transformations we obtain an alignment of the individual images to better than 0.02 – 0.04 pixels. After flag-

ging and rejecting bad pixels and cosmic rays from the input images, we created a final image for each filter, combining the input undistorted and aligned frames. The NGC 2808 and NGC 6752 final images were slightly supersampled to a pixel scale of $0''.09 \text{ pixel}^{-1}$ to mitigate the severe undersampling of these data. A square kernel was used in the final image generation and the *pixfrac* was kept near unity. M 4 has a significant number of overlapping images, so the final images were supersampled from the native resolution of $0''.13 \text{ pixel}^{-1}$ to $0''.06 \text{ pixel}^{-1}$, with a Gaussian kernel with *pixfrac* = 0.70. The FWHM on this image is ~ 2.5 pixels.

To perform the stellar photometry in M 4, we used the stand-alone versions of the DAOPHOT-II and ALLSTAR point spread function (PSF) fitting programs (Stetson 1987, 1994) on the stacked images. To obtain the final catalog we first performed aperture photometry on all the sources that are at least 3σ above the local sky. We then derived a PSF from ~ 1000 bright isolated stars in the field, and applied this PSF to all of the sources detected through the aperture photometry. We retained in the final catalogs only the sources that were iteratively matched between the two images and we cleaned them eliminating background galaxies and spurious detections by means of χ^2 and sharpness cuts from the PSF fitting. For NGC 2808 and NGC 6752, the data were too undersampled to accurately derive a PSF from the frame with DAOPHOT II. The photometry of all sources was therefore measured using an aperture with $R = 2.5$ pixels.

Photometric calibration has been performed using a sample of bright isolated stars to transform the instrumental magnitudes to a fixed aperture of 3 pixels. We then transformed the magnitudes into the VEGAMAG system by adopting the relevant synthetic zero points for the WFC3/IR filters. For NGC 2808, the final photometric source catalog is built by combining similar observations in three separate fields of the cluster. We corrected each of these fields for differential reddening prior to merging.

3. COLOR-MAGNITUDE DIAGRAMS AND FIDUCIAL LINES

Fig. 1 shows the $F110W - F160W$ vs $F110W$ CMDs for the four clusters (from left to right; 47 Tuc, M 4, NGC 2808, and NGC 6752). The derived CMDs exhibit very well defined sequences, from the sub giant branch to the low-mass MS well below the kink, which is clearly revealed in all four GCs. NGC 6752 has the shallowest photometry in our sample, but we are still able to trace the MS at least ~ 2 mag below the kink which allows us to adequately sample its shape and bending at low masses. With the exception of M 4, all of the

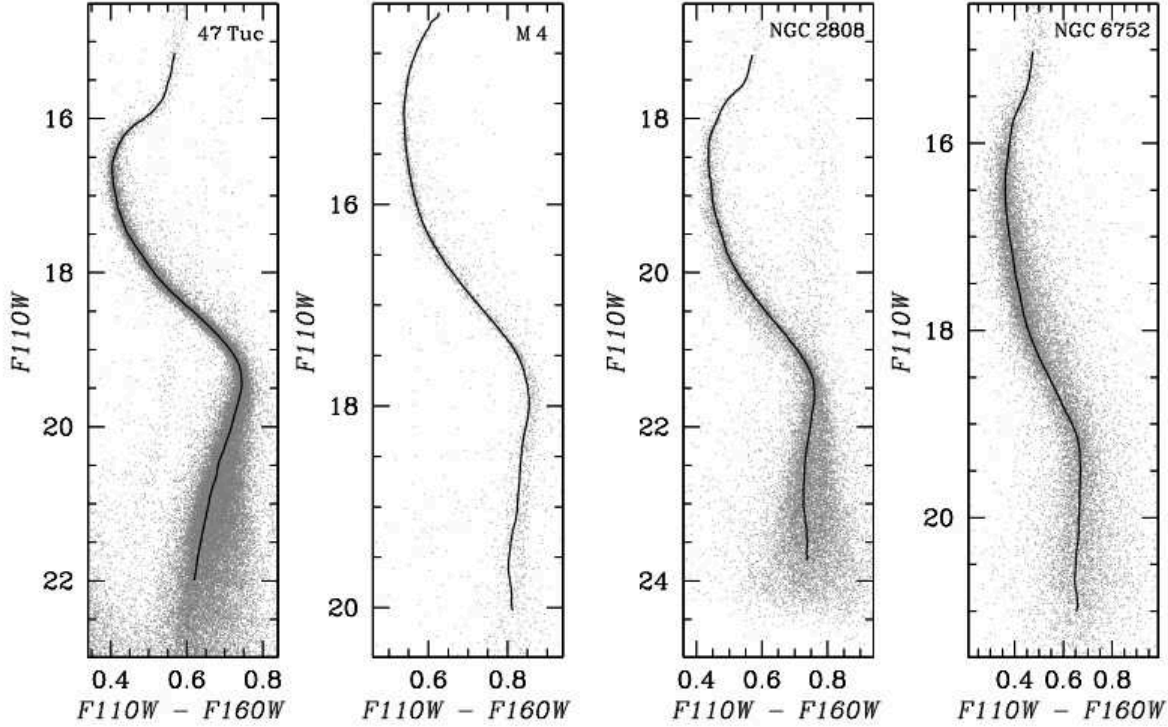


Figure 1. $F110W - F160W$ vs $F110W$ CMDs for the four clusters in our sample (from left to right panel: 47 Tuc, M4, NGC 2808, and NGC 6752), with superimposed fiducial lines (black lines) that were derived as described in Sect. 3. In contrast to simply deriving the mean color in fixed magnitude bin, the adopted approach avoids the possibility that the shape of the fiducial is altered by the presence of binaries as well as by multiple main sequences, in particular in the lower part of the MS below the kink.

cluster CMDs also sample the lower portion of the red giant branch (RGB), which offers additional leverage in simultaneously fitting models to different evolutionary stages.

The first step to obtain accurate GC parameters is to derive a fiducial line for each of the CMDs. For this, we considered the data in the $F160W$ vs. $F110W - F160W$ CMD. We used a kernel-density-estimation (KDE) to estimate the 2d PDF underlying the data. The shape of the PDF derived from the KDE can be thought of as a mountain range whose ridge represents the locus of the true underlying cluster isochrone for single stars, while the width of the range is due mostly to the measurement errors. Binaries and multiple populations also play a role in the width. We proceeded by finding the PDF global maximum, which becomes the starting point of the ridge line search. By moving along the direction of minimum gradient, we traced the ridge line. Each move was done by proposing a set of moves of fixed length within an opening cone. The move that caused the smallest drop in altitude (i.e. in PDF value) was the selected one. The length of the chosen step is related to the smoothness of the KDE PDF. For more populous CMDs, the step size can be chosen to be smaller and the resulting ridge (fiducial) line is more detailed. The walk along the ridge line was performed in two separate iterations. Starting from the same highest peak of the mountain ridge, one of these was a move towards brighter magnitudes and the other was a move towards fainter magnitudes. Once this ridge line was traced, we ensured the smoothness of the ridge line by computing the corresponding bezier curve and by using this smooth approximation instead of the previously found line.

While the direction of minimum gradient traces the underlying ridge line of the population, at each step the local direction of maximum gradient represents the direction along which the data are scattered due to measurement errors. To

estimate the actual values for the fiducial lines and their uncertainty, we adopted a bootstrap approach. We drew one thousand samples from each cluster catalog, using the same total number of stars, and allowing for repetitions. We then constructed a fiducial for each bootstrap catalog using the method outlined above. The next step was to divide the ensemble of one thousand fiducial realizations, each with about 200 points, into 0.05 mag bins in $F160W$. This bin size was chosen to ensure that each bin contains ≥ 500 points, thus minimizing Poisson noise and avoiding large bulk color changes across the bin which would otherwise artificially increase the uncertainty. We took the bin center as the $F160W$ fiducial value and half the bin size as its error. To estimate the fiducial values and their errors for the $F110W - F160W$ color, we took the mean and the standard deviation over the ensemble of fiducials, using the points that fell within each magnitude bin.

This approach offers two main advantages when compared to simply deriving the mean color in fixed magnitude bins. First, by starting from the mode of the distribution, and by moving along the most prominent range, this approach is not prone to biases due to the presence of binaries which form a mountain range that runs parallel to the main one. It also avoids the possibility that the fiducial shape is altered by the presence of multiple main sequences and ensures that the most prominent one is identified. This is particularly important in the lower part of the MS below the kink, where the separation between the different main sequences is more evident in the IR CMDs. In fact, as Milone et al. (2012, 2014) demonstrated, in NGC 2808 and M4 the MS is clearly separated in two components below the kink, due to the different chemical composition of the two sub-populations. Milone et al. (2012, 2014) suggest that the bluer MS represents a first stellar generation, having primordial helium and high oxygen, while the redder MS is associated with a second generation consisting

of stars enhanced in helium, nitrogen, sodium and depleted in oxygen.

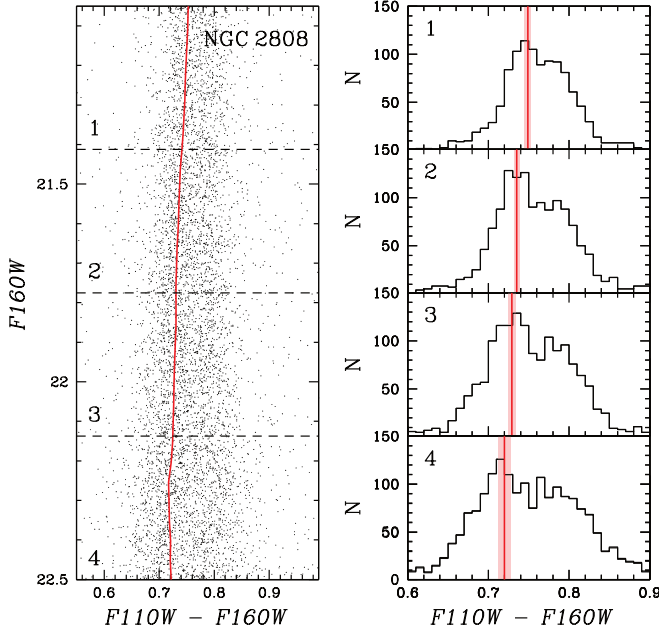


Figure 2. Left panel: zoom-in of NGC 2808 CMD in the region below the kink where the MS split is more evident. The fiducial line, derived as described in Sect. 3, is superimposed as a red curve. Right panel: color distribution of stars in the four magnitude intervals indicated by the dashed lines in the left panel. The mean fiducial color (red line) and its mean error (light red region) in each specific bin is also shown.

To verify that our method is able to accurately trace the most prominent population and to demonstrate its strength, we followed the same approach adopted by Milone et al. (2012) to identify the MS splitting below the kink. The left panel of Fig. 2 shows a zoom-in of the NGC 2808 CMD below the kink, where the MS split is more evident. The derived fiducial line is superimposed in red. The color distribution of stars in the four magnitude intervals, over the range $21.05 < F160W < 22.5$ mag, are shown in the right panels. The mean fiducial color (red line) and its mean error (light red region) in the specific bin is also shown. The distribution is clearly bimodal, with an overall shape similar to the one found by Milone et al. (2012). The different number of stars in each bin is caused by different choices in the selection of the sample, and the mean color of the fiducial line is almost coincident with the peak of the distribution in each bin. Hence, Fig. 2 confirms that the adopted method successfully traces the most prominent population of the cluster when more than one main sequence is present.

To derive the “genuine” GC parameters, it is important to trace the primordial “first generation” population that has the original cluster chemical abundance. In NGC 2808, the first stellar generation is also the most populated one, but this is not the case in M4. As pointed out by Milone et al. (2014) and shown in the right panel of Fig. 3, the blue sequence in M4 is less populated than the red one. Hence, for this cluster, our method does not properly derive the fiducial line of the cluster below the kink. To overcome this issue, we adopted the following empirical approach: we applied a magnitude-color cut in the CMD to select the stars fainter than $F160W \sim 17$ mag where the split between the two sequences begins. The

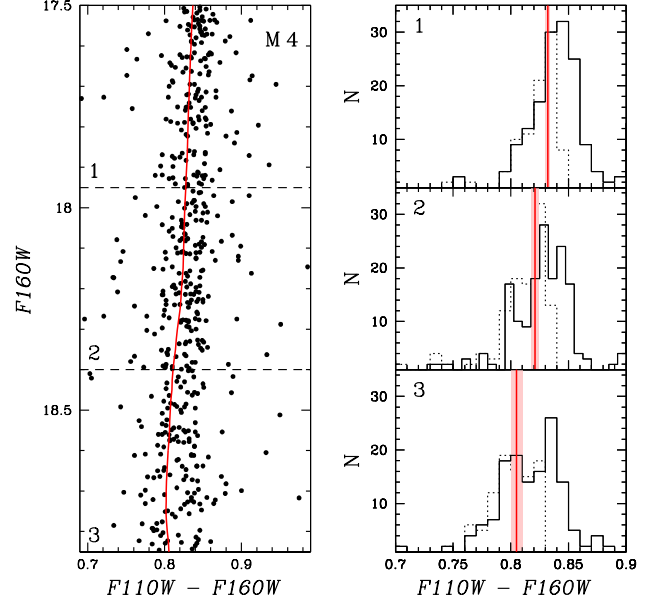


Figure 3. Same as Fig. 2 but for the cluster M4. In the case of M4, the primordial population is not the most populous one, therefore we have modified the fiducial line computation mechanism to follow the secondary ridge of the density distribution and not the primary, as shown in the right panel (see text for details). The dotted histograms represent the color distribution of stars in the three magnitude intervals after applying the magnitude-color cut described in Sect. 3.

cut is made to select stars that are redder than the quantity $(F110W - F160W)_{fiducial} + \sigma$, where $(F110W - F160W)_{fiducial}$ is the color of the fiducial line that traces the most prominent population and σ is its error. We then removed these objects from the M4 catalog and re-derived the fiducial line and its error on the new dataset. We iterated this procedure by applying different magnitude cuts through a ± 0.25 mag step with respect to the default quoted above, and verified that the derived fiducial lines are consistent with each other within the errors and that the shape is not altered by the different selection choices. The resulting color histograms (dotted line) for each magnitude bin are reported in the right panel of Fig. 3, together with the mean fiducial color (red line) and its mean error (light red region). With the exception of the central magnitude interval, for which the mean color of the fiducial is still too red compared to the color of the blue peak of the first stellar generation, the newly derived fiducial line reproduces quite well the observed distribution. However, as we will see in Sect. 4.2, this small discrepancy does not affect the global fitting and the resulting best-fit parameters for M4. Due to the different procedure applied for this cluster and the low number of stars below the kink, the uncertainties derived in Sect. 4.3 could be slightly underestimated.

Tracing the primordial MS below the kink is an important factor in deriving the correct cluster metallicity and therefore a precise age estimate. In fact, the degree of the MS bending is strictly related to the cluster metallicity, due to the different opacities in stars. The net effect is that more metal-rich clusters will exhibit a MS bending that is more accentuated bluewards. This effect is clearly visible in the fiducial lines shown in Fig. 1: as expected, the more metal-rich GC of our sample (i.e., 47 Tuc, $[Fe/H] \simeq -0.75$ dex, left panel of Fig. 1) exhibits a fiducial line which is clearly more tilted bluewards

Table 2
GC prior parameters and ranges

Cluster (1)	Age _{range} (2)	[Fe/H] (3)	Δ [Fe/H] (4)	ref. (5)	$(m-M)_0$ (6)	$\Delta (m-M)_0$ (7)	E(B-V) (8)	E(B-V) _{range} (9)	ref. (10)
47 Tuc	9.0–15.0	-0.77	± 0.20	1	13.24	± 0.25	0.04	0.00–0.20	1
M 4	9.0–15.0	-1.12	± 0.20	2	11.28	± 0.25	0.37	0.22–0.52	2
NGC 2808	9.0–15.0	-1.22	± 0.20	3	14.91	± 0.25	0.19	0.04–0.34	1
NGC 6752	9.0–15.0	-1.55	± 0.20	4	13.01	± 0.25	0.04	0.00–0.19	1

Note. — Columns (1): Name of the clusters. (2): Age interval (Gyr). (3): Metallicity reference value (dex). (4): Metallicity interval (dex). (5): Reference for the metallicity value ((1) Carretta et al. (2009b, and references therein); (2) Marino et al. (2011); (3) Marino et al. (2014); (4) Carretta et al. (2009b, and references therein). (6): Distance modulus reference value (mag). (7): Distance modulus interval (mag). (8): Reddening reference value (mag). (9): Reddening interval (mag). (10) Reference for distance modulus and reddening values. ((1) Harris (2006, updated as in 2010); (2) Hendricks et al. (2012)).

than the others. Moving towards lower metallicity (from the left to the right CMDs in Fig. 1), the fiducial lines bending shifts progressively redwards, until in the most metal-poor GC of our sample (i.e., NGC 6752, [Fe/H] \simeq -1.5 dex, right panel of Fig. 1) there is essentially no bending and the sequence is vertical.

4. CONSTRAINTS ON THE GC PARAMETERS

4.1. Isochrone fitting: deriving ages

To derive the age, metallicity, distance and reddening for the four GCs, we compared the fiducial lines (obtained as described in Sect. 3) with a set of stellar models from the Victoria-Regina stellar evolution code (VandenBerg et al. 2014). The models were transformed to the WFC3/IR filter system by performing synthetic photometry using the MARCS library of stellar spectra (Gustafsson et al. 2008) and the most updated WFC3/IR throughputs and zero points. Extinction was taken into account by applying the Fitzpatrick (1999) extinction law to the spectra before integrating them under the throughput curves, using the appropriate R_V value for each cluster.

We constructed a grid of isochrones over a large range of parameter space that allowed age, metallicity, distance and reddening to vary over reasonable ranges. The reference values and the adopted intervals are reported in Table 2. We use a fixed age range from 9 to 15 Gyr for all GCs, whereas for the metallicity, we used an interval of ± 0.20 dex with respect to literature values derived from spectroscopic studies for each cluster. For the distance modulus, we adopted an interval of ± 0.25 mag. For the reddening, we used $E(B-V) = 0$ as a lower limit and $E(B-V)_{ref} + 0.15$ mag as an upper limit (with the exception of M4, for which we adopted an interval of ± 0.15 mag from the reference value). When necessary, we iteratively readjusted the parameter range in order to center the derived best-fit results in the new interval. The derived grid is obtained by adopting steps of 0.1 Gyr for the age, 0.01 dex for the metallicity and 0.01 mag for distance and reddening. We assume that, within the allowed ranges, the prior probability distribution of the parameters is uniform.

In our analysis, the only a priori fixed parameters are the $[\alpha/\text{Fe}]$ ratio, the extinction coefficient R_V and the helium abundance. For the $[\alpha/\text{Fe}]$ ratio we adopted the value $[\alpha/\text{Fe}] = +0.4$, as suggested from spectroscopic studies of these clusters. For the extinction coefficient, R_V , we adopted the value $R_V = 3.1$ for all GCs except for M4, for which we adopted a higher value of $R_V = 3.6$ (Hendricks et al. 2012). The original helium abundance in the stellar models was obtained using Eq. 1 and Eq. 2 from Gennaro et al. (2010), after the ratio between [Fe/H] and [M/H] was taken into account using Eq. 3 from Salaris et al. (1993). We assumed the solar mixture from Asplund et al. (2009), a primordial helium abundance

of $Y_p = 0.2485$ from Izotov et al. (2007) and Peimbert et al. (2007), and a ratio of $\Delta Y / \Delta Z = 1.5$.

To obtain the best-fit isochrone for each cluster, we compared the fiducial lines with the isochrone grid, deriving for each isochrone the posterior PDF which, due to the choice of uniform priors for our parameters, is proportional to the likelihood \mathcal{L} . The latter is calculated using the following equation:

$$\mathcal{L} \simeq \exp\left(-\frac{1}{2}\chi^2\right) \quad (1)$$

where the term χ^2 in Eq. 1 is defined as:

$$\chi^2 = \sum_{i=1}^N \frac{(\Delta col_i)^2}{\sigma_i^2} \quad (2)$$

where Δcol is the difference in color between the isochrones and the fiducial (i.e. $(F110W - F160W)_{iso} - (F110W - F160W)_{fiducial}$), calculated at each point in the fiducial line. σ is the error associated with the fiducial color points, derived as described in Sect. 3. The best-fit isochrone is the one that maximizes the joint PDF for the four parameters.

Fig. 4 shows the GC CMDs (ordered as in Fig. 1) with superimposed fiducial lines (black lines) and the best-fit isochrones (red lines). The derived parameters and uncertainties from the best-fit isochrone for each cluster (i.e., age, metallicity, distance modulus, and reddening – as described in Sect. 4.3) are reported in Table 3. The best-fit isochrones reproduce almost perfectly the fiducial lines along all of the sequences in the CMDs. To better visualize the goodness of the fit, we illustrate the fit residuals (i.e., the term Δcol in Eq. 2) in Fig. 5 as a function of the magnitude F110W for the four GCs (47 Tuc, top left panel, M4, top right panel, NGC 2808, bottom left panel, and NGC 6752, bottom right panel). The 1σ and 2σ errors (dark and light gray area in Fig. 5), where σ is the fiducial color error as defined above, are also presented in Fig. 5. Small discrepancies between the fiducial line and the best-fit isochrone, of the order of few hundredths of a magnitude, are observed in the sub giant branch and red giant branch of 47 Tuc and in the red giant branch of NGC 6752. However, in the latter case, we note that due to the paucity of stars populating this region of the CMD, the fiducial line colors can not be determined with high precision. For M4, we derived the best-fit parameters using also the other two fiducial lines obtained with the different magnitude cuts, as described in Sect. 3. We obtained variations of just ± 0.2 Gyr for the age, ± 0.02 dex for the metallicity, ± 0.01 mag for the distance modulus, and ± 0.01 mag for the reddening, with respect to the value reported in Table 3.

4.2. Comparison with literature estimates

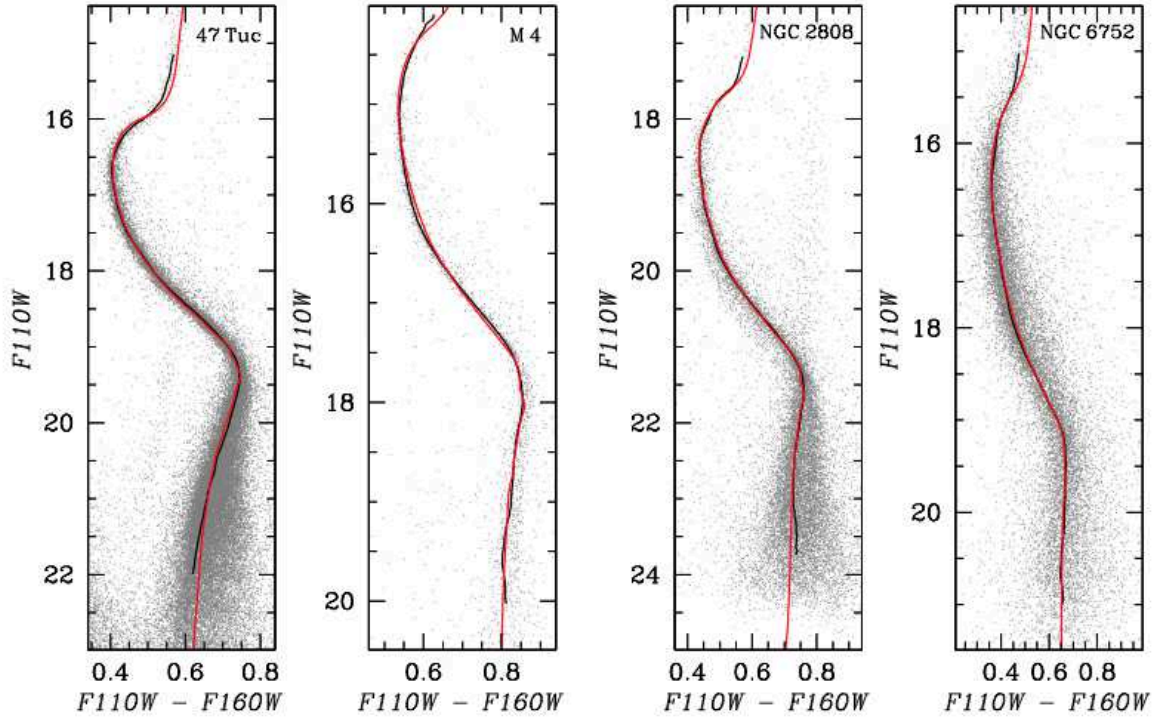


Figure 4. $F110W - F160W$ vs $F110W$ CMDs for the four clusters in our sample (from left to right panel: 47 Tuc, M4, NGC 2808, and NGC 6752), with superimposed fiducial lines (black lines) and the best-fit isochrones derived as described in Sect. 4.2. Best-fit parameters are reported in Table 3.

Table 3
GC parameter estimates

Cluster (1)	Age (2)	σ (3)	[Fe/H] (4)	σ (5)	$(m-M)_0$ (6)	σ (7)	E(B-V) (8)	σ (9)
47 Tuc	11.6	$^{+0.7}_{-0.7}$	-0.69	$^{+0.8}_{-0.8}$	13.31	$^{+0.04}_{-0.05}$	0.04	$^{+0.01}_{-0.02}$
M4	11.5	$^{+0.5}_{-0.5}$	-1.09	$^{+0.06}_{-0.04}$	11.35	$^{+0.03}_{-0.04}$	0.38	$^{+0.01}_{-0.02}$
NGC 2808	11.2	$^{+1.1}_{-0.7}$	-1.23	$^{+0.07}_{-0.11}$	15.09	$^{+0.04}_{-0.06}$	0.21	$^{+0.02}_{-0.03}$
NGC 6752	12.1	$^{+1.0}_{-1.2}$	-1.50	$^{+0.08}_{-0.13}$	13.11	$^{+0.06}_{-0.06}$	0.02	$^{+0.03}_{-0.02}$

Note. — Columns (1): Name of the clusters. (2): Age (Gyr). (3): Age uncertainty (Gyr, 68% confidence interval). (4): Metallicity (dex). (5): Metallicity uncertainty (dex, 68% confidence interval). (6): Distance modulus (mag). (7): Distance modulus uncertainty (mag, 68% confidence interval). (8): Reddening (mag). (9) Reddening uncertainty (mag, 68% confidence interval).

To verify that the isochrone fitting provides reasonable values for the best-fit parameters, we compared our results with literature estimates of these four GCs. The most direct comparison is with the results obtained by VandenBerg et al. (2014), but, unfortunately, there is only one cluster in common between the two studies, namely 47 Tuc. Hence, we focus on the results obtained by VandenBerg et al. (2013), who derived the same parameters from the analysis of HST Advanced Camera for Survey (ACS) visible light photometry. This analysis used the same stellar evolutionary code that we use, although slightly different prescriptions for the isochrone computation. Briefly, the main difference between the two sets of models concerns the assumed metal mixture, that is VandenBerg et al. (2014) models assume a significantly lower abundance of the CNO elements (see for a detailed description of the models and their differences, VandenBerg et al. 2013, 2014). This, in turn, implies that slightly higher ages will be obtained using VandenBerg et al. (2014) models, with respect to those derived by VandenBerg et al. (2013), due to the fact

that turn-off luminosity versus age relations depend on the absolute abundance of oxygen (see for an exhaustive discussion, VandenBerg et al. 2012). In this context, VandenBerg et al. (2014) specified that to partially compensate for the expected effects of the different oxygen and metal abundances between the models, they assumed slightly larger distance moduli (≤ 0.05 mag) and ages (by 0.25 Gyr) with respect to the values derived by VandenBerg et al. (2013). We can then assume that a similar variation, of the order of 0.25–0.75 Gyr (depending on the assumed apparent distance modulus), can be expected also for the clusters in this work that were not analyzed in VandenBerg et al. (2014); therefore, the ages reported in VandenBerg et al. (2013) should be increased by these quantities in order to obtain ages based on VandenBerg et al. (2014) isochrones. We note that, also taking into account these variations, our age estimates are in agreement within the errors with those derived by VandenBerg et al. (2013). In the following, to not generate confusion to the readers, we will report the original values derived by VandenBerg et al. (2013),

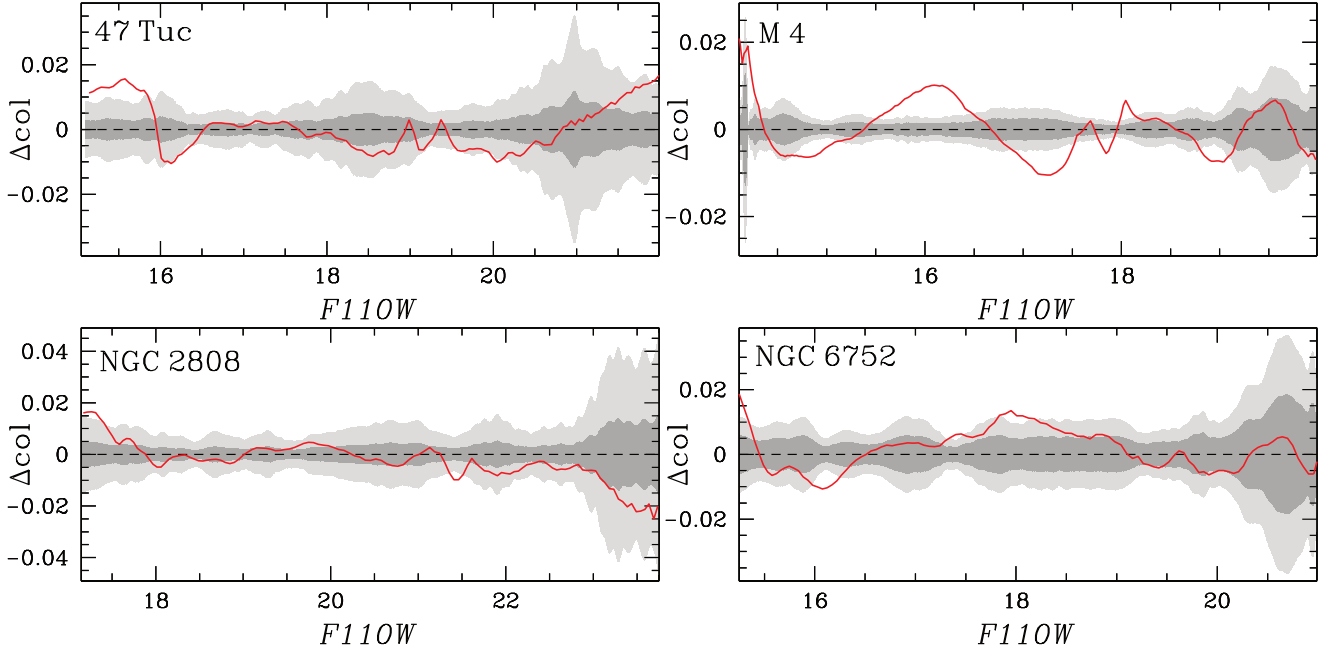


Figure 5. Residuals of the fit between the best-fit isochrone and the fiducial line for the four clusters (Top left panel: 47 Tuc; top right panel: M 4; bottom left panel: NGC 2808; bottom right panel: NGC 6752). Dark and light gray areas represent the 1σ and 2σ fiducial color errors respectively.

with the exception of 47 Tuc for which we report the values derived in VandenBerg et al. (2014).

We briefly summarize these comparisons.

47 Tuc: the best-fit parameters for this cluster are in good agreement within the errors with the values derived by VandenBerg et al. (2014). They derived an age of 12.0 Gyr and an apparent distance modulus $(m-M)_V = 13.40$ mag, assuming a metallicity $[\text{Fe}/\text{H}] = -0.76$ dex and reddening $E(\text{B}-\text{V}) = 0.028$ mag⁴. Our best-fit parameters are also in good agreement with the Harris (2006) database; $[\text{Fe}/\text{H}] = -0.72$ dex, $(m-M)_V = 13.37$ mag and $E(\text{B}-\text{V}) = 0.04$ mag.

M 4: the derived values for M 4 are in good agreement with the values derived by VandenBerg et al. (2013), with the exception of the metallicity.

Within the uncertainty, we derive the same age (11.5 Gyr) and apparent distance modulus $((m-M)_V = 12.72$ mag vs $(m-M)_V = 12.74$ mag) as VandenBerg et al. (2013), but the metallicity is slightly different ($[\text{Fe}/\text{H}] = -1.09$ dex vs $[\text{Fe}/\text{H}] = -1.18$ dex). However, the metallicity estimates of M 4 derived from high-resolution spectroscopy cover this range; for example, $[\text{Fe}/\text{H}] \simeq -1.07$ dex (Marino et al. 2008; Villanova et al. 2012; Malavolta et al. 2013) to $[\text{Fe}/\text{H}] \simeq -1.18$ (Ivans et al. 1999; Carretta et al. 2009a). As shown in Table 2, we adopted $[\text{Fe}/\text{H}] = -1.12$ dex (Marino et al. 2011) as a reference value.

The M 4 dataset in our study is optimized to achieve high-precision photometry for faint M-dwarfs. As a result, we were not able to sample the RGB and could not achieve a stronger constraint on the cluster metallicity from CMD fitting. Still, the derived metallicity is in good agreement with the literature values, suggesting that the luminosity of the kink and the bending of the low-mass MS could provide a new diagnostic for this parameter. Distance determination also agrees quite well with the recent estimates based on RR Lyraes $((m-M)_0 = 11.27-11.39$ mag, Neeley et al. 2015; Braga et al. 2015, see their Table 1 for a detailed summary of the distance and red-

dening available in the literature). Taking into account the derived reddening $E(\text{B}-\text{V}) = 0.38$ mag and the adopted $R_V = 3.6$, we obtain an apparent distance modulus $(m-M)_V = 12.72$ mag. Since $\langle M_V \rangle = 13.33$ mag for the RR Lyrae in M 4 (Braga et al. 2015), we obtain a $\langle M_V \rangle = 0.61$ mag. Clementini et al. (2003) results for the apparent magnitude of the Large Magellanic Clouds (LMC) RR Lyrae as a function of $[\text{Fe}/\text{H}]$ coupled with the very precise LMC distance found by Pietrzyński et al. (2013) yields $\langle M_V \rangle = 0.66 \pm 0.06$ mag for RR Lyrae that have $[\text{Fe}/\text{H}]$ values near -1.1 dex, in agreement within the errors with the $\langle M_V \rangle$ derived in this work.

NGC 2808: While the best-fit parameters for age, metallicity, and reddening are in good agreements with VandenBerg et al. (2013), the apparent distance modulus does not agree. Our value is $(m-M)_V = 15.74$ mag, 0.15 mag larger than the VandenBerg et al. (2013) estimate of $(m-M)_V = 15.59$ mag (coincident with the value tabulated in Harris 2006). Using a different stellar model grid (BaSTI, Pietrinferni et al. 2004, 2006) and a slightly different chemical composition ($[\alpha/\text{Fe}] = +0.3$ dex), Marino et al. (2014) fitted the cluster using an isochrone with age 10 Gyr, metallicity $[\text{Fe}/\text{H}] = -1.15$ dex, apparent distance modulus $(m-M)_V = 15.67$ mag, and reddening $E(\text{B}-\text{V}) = 0.19$ mag. This latter value for the distance is in agreement within the errors with our estimate, although from the distance-age relation we should expect to obtain a younger age given our larger distance estimate. As another example, Dalessandro et al. (2011), used high-resolution far-UV and optical images of the central region of the cluster from HST/WFPC2 to analyze the horizontal branch of the cluster. Using the same set of isochrones as in Marino et al. (2014), they derived an age of 12 Gyr, a metallicity $[\text{Fe}/\text{H}] = -1.31$ dex, and an $[\alpha/\text{Fe}] = +0.4$ dex. They measured an apparent distance modulus $(m-M)_V = 15.74$ mag, the same as that derived in our study.

NGC 6752: best-fit parameters are in agreement within the uncertainties with the results obtained by VandenBerg et al. (2013), who derived an age of 12.5 Gyr and apparent distance modulus $(m-M)_V = 13.24$ mag, assuming a metallicity $[\text{Fe}/\text{H}]$

⁴ VandenBerg et al. (2013) and VandenBerg et al. (2014) adopted $[\text{Fe}/\text{H}]$ values from Carretta et al. (2009b) and $E(\text{B}-\text{V})$ values, with few exceptions, from Schlegel et al. (1998).

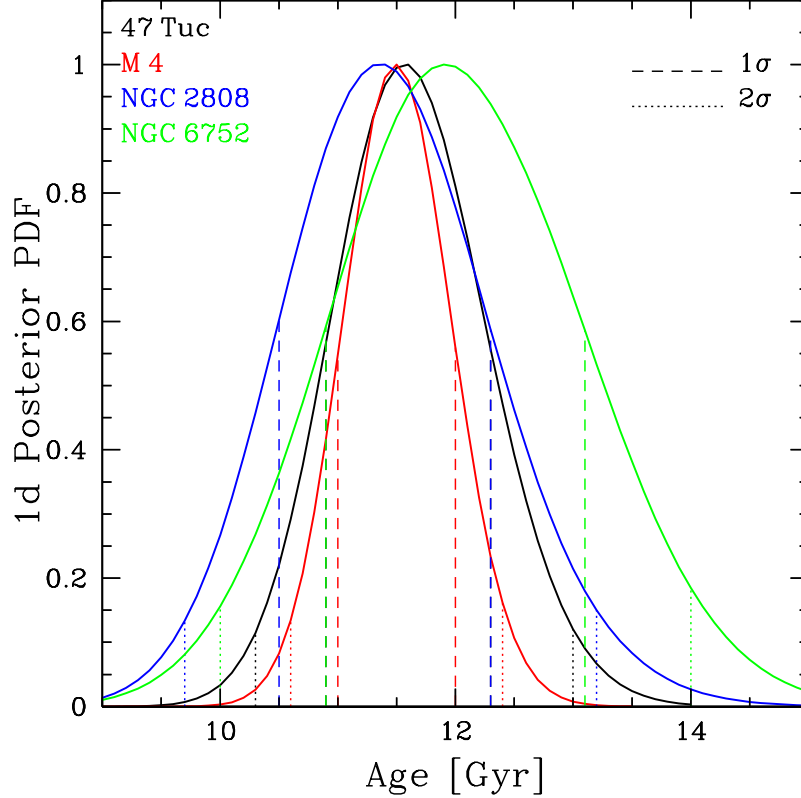


Figure 6. 1d posterior PDFs of the age for the four GCs (Black line: 47 Tuc; red line: M 4; blue line: NGC 2808; green line: NGC 6752) obtained by marginalizing the 4d PDFs over metallicity, distance and reddening. 1σ (dashed lines) and 2σ (dotted lines) confidence intervals, defined as described in Sect. 4.3, are also shown.

$= -1.55$ dex and reddening $E(B-V) = 0.056$ mag. Our distance value is also in good agreement with the value tabulated in Harris (2006) database, $(m-M)_V = 13.13$ mag.

4.3. Posterior probability density function: deriving age uncertainties

As we stated in Sect. 1, the main advantage of using the MS kink in IR CMDs as an age diagnostic is that this feature can provide a fundamental tool to reduce the uncertainties associated with GC age estimates. The location of the kink and the shape of the bending of the low-mass MS are dependent on metallicity, but are independent of age, allowing a partial break of the degeneracy between these two parameters. Due to the particular shape of the color-magnitude relation below the kink, the uncertainties related to the distance and reddening are also reduced.

To test the validity of this hypothesis and accurately derive the age uncertainties for each cluster, we adopted the following approach. For each isochrone of the grid, we derived the joint posterior PDF, which, as stated in Sect. 4.2, due to the choice of uniform priors for our parameters, is proportional to the likelihood \mathcal{L} . The latter is derived from Eq. 1 and Eq. 2. We then derived the 1d posterior PDF for the age, obtained by the marginalization of the 4d PDF (i.e., $P(\text{age}, \text{metallicity}, \text{reddening}, \text{distance})$) over metallicity, distance and reddening. The 1d posterior PDFs for the four GCs are shown in Fig. 6 (47 Tuc, black line, M 4, red line, NGC 2808, blue line, and NGC 6752, green line, respectively). The age uncertainties are derived from the cumulative

distribution of the marginalized age distribution; 1σ (2σ) confidence intervals are defined as the area enclosed within 16% (2.5%) and 84% (97.5%) of each cluster’s cumulative distribution. This would correspond to the *true* 1σ and 2σ uncertainties if the 1d PDFs were Gaussian. Fig. 6 shows that the derived random age uncertainties are of the order of $\sigma \sim 0.7 - 1.1$ Gyr. As stated in Sect. 3 and considering the uncertainties in the best-fit parameters for M 4 when a different magnitude cut is applied, we acknowledge that the derived uncertainty for the age of this cluster, $\sigma = 0.5$ Gyr, could be underestimated. Taking into account the age range derived in Sect. 4.2, and considering a systematic uncertainty of the order of ± 0.3 Gyr, we estimate that the value $\sigma \sim 0.8$ Gyr is more representative of the GC age uncertainty. Similar uncertainties, of the order of ± 1 Gyr, have been recently derived by Monelli et al. (2015), which exploited the MS kink as a diagnostic to derive the absolute age of the old metal-poor GC M 15. Their analysis is based on near-IR images collected with the PISCES camera, coupled with the First Light Adaptive Optics system mounted at the Large Binocular Telescope.

To better visualize how the use of the kink lessens the correlations and interdependencies between the various parameters, we derived the 2d posterior PDFs of all of the parameters for each cluster. These 2d PDFs are obtained as described above, with the only difference being that the 4d PDF is marginalized over two parameters instead of three. For example, the 2d PDF of age and metallicity is obtained by marginalization of the 4d PDF over distance and reddening. Fig. 7 shows 47 Tuc 2d posterior PDFs, Fig. 8 M 4 2d poste-

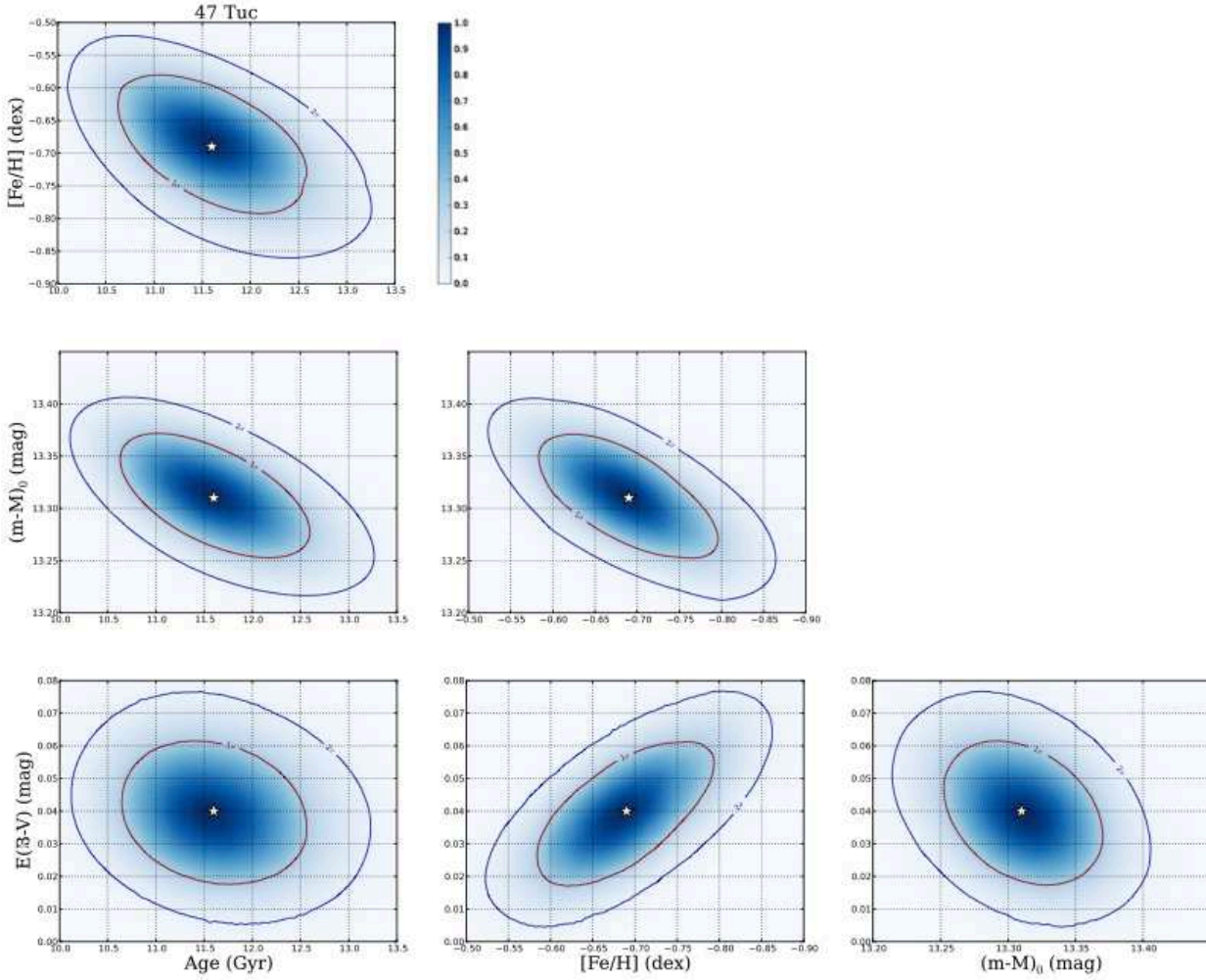


Figure 7. 2d posterior PDFs of all of the parameter combinations for 47 Tuc (upper panel: age vs metallicity 2d PDF; middle panels: age vs distance modulus, metallicity vs distance modulus 2d PDFs; lower panels: age vs reddening, metallicity vs reddening, and distance modulus vs reddening 2d PDFs). The 1σ (red lines) and 2σ (blue lines) regions are defined as the smallest regions such that the integral of the 2d PDFs within the regions are equal to 0.68 and 0.95. Color codes for the 2d PDFs are shown in the upper right sub-panel. The white stars indicate the values for which the 4d PDF has a maximum.

prior PDFs, Fig. 9 NGC 2808 2d posterior PDFs, and Fig. 10 NGC 6752 2d PDFs. In particular, the distance vs reddening 2d PDFs (bottom right panel in each Figure) shows that the morphology of the color-magnitude relation in the low mass-MS leads to a decrease in the uncertainties on distance and reddening, and consequently on the GC ages.

These uncertainties can be considered to be an upper limit as they are obtained adopting a conservative approach that assumes a priori uniform distributions over the allowed parameter ranges. If we adopted stronger constraints from independent measures of these parameters, the derived age uncertainty would be lower. Finally, we note that the quoted uncertainties only take into account random noise (number statistics and measurement errors). We acknowledge that the total uncertainty on GC parameters is further increased by the presence of a systematic component due to e.g. the choice of the stellar evolution library, stellar atmospheres and possible zero-point offsets (as well as other, more subtle, possibly unknown sources of uncertainty).

The results from this project suggest that using IR photometry and the kink as an age diagnostic can push the absolute ages of GCs to sub-Gyr accuracy with the next generation near-IR telescopes, such as the *James Webb Space Telescope* (JWST), the *Wide Field Infrared Survey Telescope* (WFIRST),

and large ground-based telescopes with advanced adaptive optics technology.

5. SUMMARY AND CONCLUSIONS

In this study, we investigated the predictive power and the constraints established on GC properties by leveraging the shape of the MS color-magnitude relation in pure IR CMDs. The IR color-magnitude relation exhibits a kink due to opacity effects in M dwarfs, such that low mass MS stars become bluer in the IR color baseline and not redder. The combination of the MS turn-off location with that of the MS kink, and the shape of the bending below the kink, decreases the effects of the correlations and interdependencies between various parameters (i.e., age, metallicity, distance and reddening). Therefore, this diagnostic offers a new opportunity to improve the accuracy of GC age measurements over visible-light studies.

We analyzed publicly available MAST data for four GCs, namely 47 Tuc, M4, NGC 2808, and NGC 6752, for which existing data are deep enough to reach $\simeq 2$ mag below the kink. With this photometry, we can fully sample the bending of the MS at low masses.

By using an ad-hoc fitting method, we derived fiducial lines for the four GCs. We compared them with a grid of

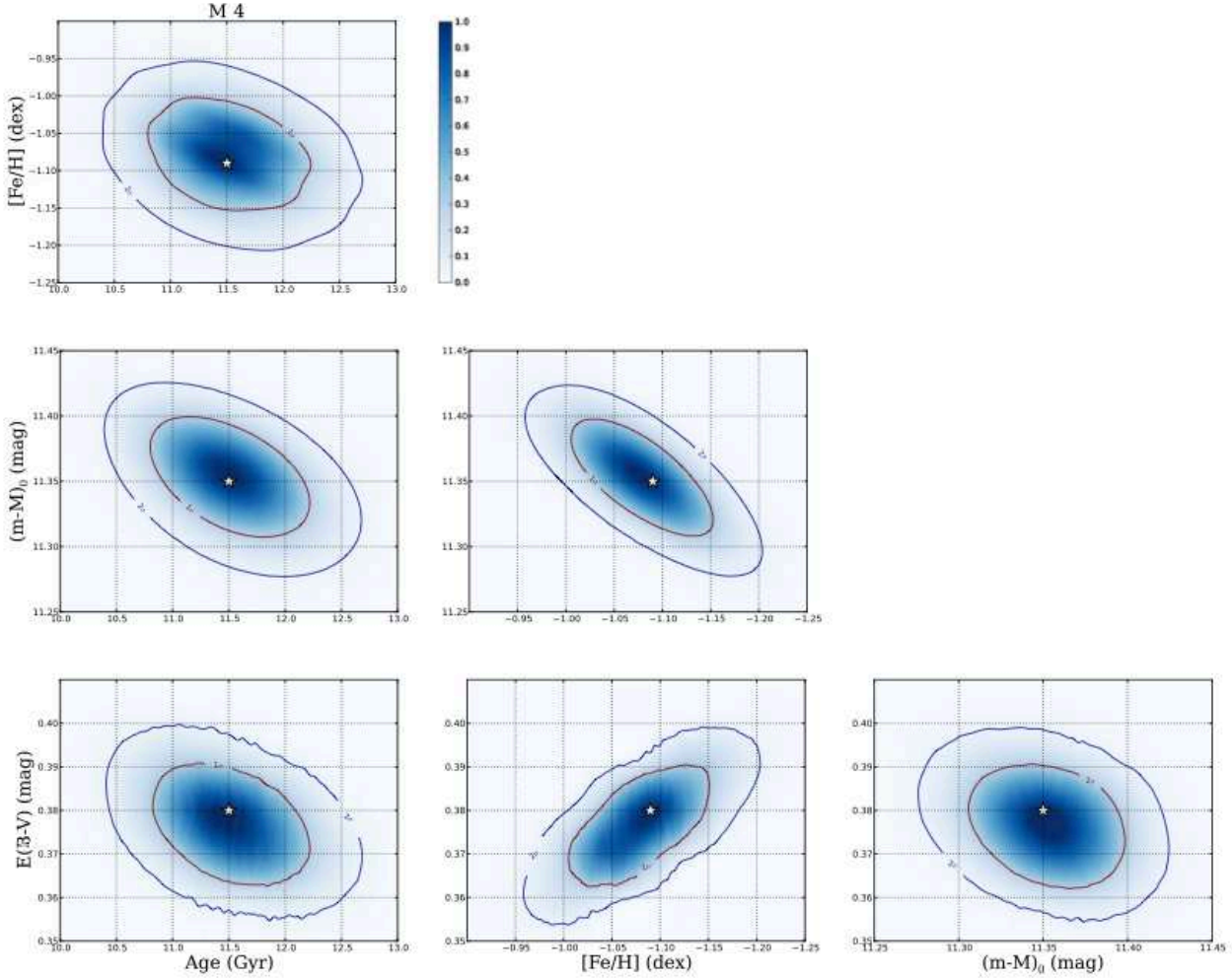


Figure 8. Same as Fig. 7, for the GC M 4

isochrones over a large range of parameter space that allows age, metallicity, distance, and reddening to vary within reasonably selected ranges. We calculated the joint posterior PDF for the four parameters, and derived best fit isochrones by maximizing the PDF. We obtained an age of 11.6 Gyr for 47 Tuc, 11.5 Gyr for M4, 11.2 Gyr for NGC 2808, and 12.1 Gyr for NGC 6752. These best-fit ages, and the other derived parameters, agree quite well with the results obtained by VandenBerg et al. (2013), who used the same stellar evolution code to analyze visible-light ACS photometry of these GCs.

To derive the age uncertainty in each GC, we calculated the 1d posterior PDF, obtained by marginalizing the 4d posterior PDF over metallicity, distance and reddening. We calculated the 1σ and 2σ confidence intervals from the cumulative distribution of the marginalized 1d PDF, where $1(2)\sigma$ is defined as the area enclosed within the 16% (2.5%) and 84% (97.5%) of the cumulative distribution. The random age uncertainties are $\sigma \sim 0.7 - 1.1$ Gyr. Our results suggest that the IR color-magnitude relation and kink in the lower MS represents a promising tool to obtain absolute ages of GCs with sub-Gyr accuracy.

Deriving sub-Gyr ages for GCs represents a foundation for many astrophysical topics. A precise age will constrain the formation epoch of clusters with respect to reionization, which is crucial for constraining models of cluster formation.

More accurate ages will also lead to a new age-metallicity relation with absolute uncertainty that is smaller than the current scatter. Obtaining sub-Gyr ages for GCs will enable us to accurately derive the *absolute* normalization and the slope of this relation. The latter is an anchor to high-resolution N-body simulations of galaxy formation, and informs the mass-merger history that leads to the build up of Milky Way-type halos (Mackey & Gilmore 2004; Beers et al. 2012, and references therein).

Producing an accurate set of fiducial lines, spanning a large range of metallicity, is of fundamental importance both from the theoretical and observational point of view. These relations can help test stellar models for low mass stars and represent fundamental templates for the calibration of future space observations with the next generation near-IR telescopes, such as JWST, WFIRST, and ground-based 30-meters telescopes with adaptive optics technology.

We are grateful for a very thoughtful review by the anonymous referee, which improved this paper.

REFERENCES

- Asplund, M., Grevesse, N., Sauval, A. J., & Scott, P. 2009, ARA&A, 47, 481
- Beers, T. C., et al. 2012, ApJ, 746, 34
- Bono, G., et al. 2010, ApJ, 708, L74
- Braga, V. F., et al. 2015, ApJ, 799, 165
- Brodie, J. P., & Strader, J. 2006, ARA&A, 44, 193

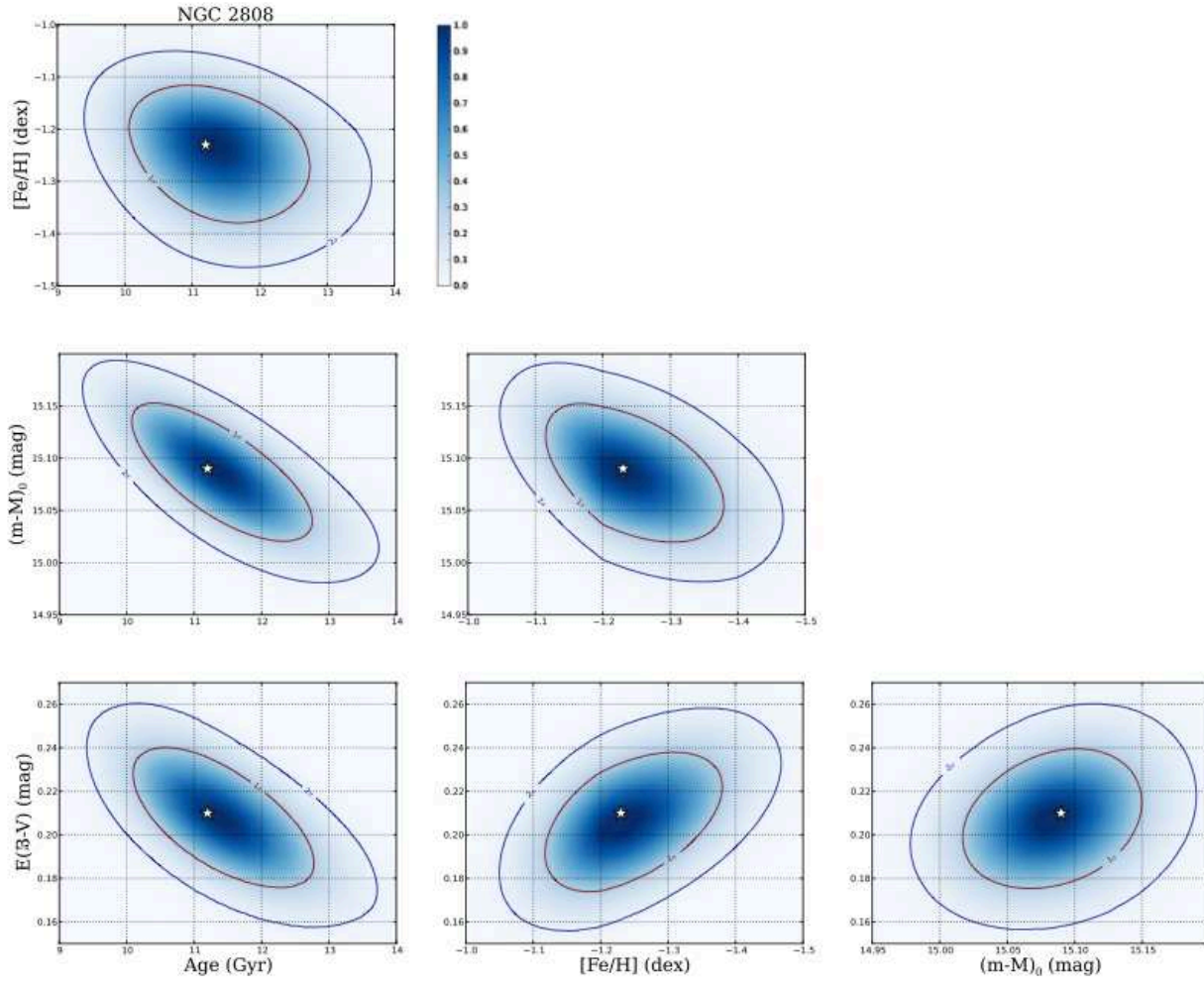


Figure 9. Same as Fig. 7, for the GC NGC 2808

- Calamida, A., et al. 1999, *IAUS*, 258, 189
 Carretta E., et al. 2009, *A&A*, 505, 117
 Carretta, E., Bragaglia, A., Gratton, R., D'Orazi, V., & Lucatello, S. 2009, *A&A*, 508, 695
 Cassisi, S., Castellani, V., degl'Innocenti, S., Salaris, M., & Weiss, A. 1999, *A&A*, 134, 103
 Chaboyer, B., & Krauss, L. 2002, *ApJ*, 567, 45
 Chaboyer, B. 2008, *IAU Symp.*, 248, 440
 Clementini, G., Gratton, R. G., Bragaglia, A., Carretta, E., Di Fabrizio, L., & Maio, M. 2003, *AJ*, 125, 1309
 Dalessandro, E., Salaris, M., Ferraro, F. R., Cassisi, S., Lanzoni, B., Rood, T. R., Fusi Pecci, F., & Sabbi, E. 2011, *MNRAS*, 410, 694
 Dotter, A., Chaboyer, B., Jevremovic, D., Kostov, V., Baron, E., & Ferguson, J. W. 2008, *ApJS*, 178, 89
 Fitzpatrick, E. L. 1999, *PASP*, 111, 63
 Fruchter, A. S., & Hook R. N. 2002, *PASP*, 114, 144
 Gennaro, M., Prada Moroni, P. G., & Degl'Innocenti, S. 2010, *A&A*, 518, 13
 Grundahl, F., VandenBerg, D. A., & Andersen, M. I. 1998, *ApJ*, 500, 179
 Gustafsson, B., Edvardsson, B., Eriksson, K., Jorgensen, U. G., Nordlund, A., & Plez, B. 2008, *A&A*, 486, 951
 Hansen, B. M. S., et al. 2013, *Nature*, 500, 51
 Harris, W. R. 1996, *AJ*, 112, 1487
 Hendricks, B., Stetson, P. B., VandenBerg, D. A., & Dall'Ora, M. 2012, *AJ*, 144, 25
 Kalirai, J. S., et al. 2012, *AJ*, 143, 11
 Iben, I., & Renzini, A. 1984, *phRep*, 105, 329
 Ivans, I. I., Sneden, C., Kraft, R. P., Snutzef, N. B., Smith, V. V., Langer, G. E., & Fullbright, J. P. 1999, *AJ*, 118, 1273
 Izotov, Y. I., Thuan, T. X., & Stasińska, G. 2007, *ApJ*, 662, 15
 Linsky, J. L. 1969, *AJ*, 156, 989
 Mackey, A. D., & Gilmore, G. F. 2004, *MNRAS*, 355, 504
 Malavolta, L., Sneden, C., Piotto, G., Milone, A. P., Bedin, L. R., & Nascimbeni, V. 2013, *AJ*, 147, 25
 Marino, A. F., Villanova, S., Piotto, G., Milone, A. P., Momany, Y., Bedin, L. R., & Medling, A. M. 2008, *A&A*, 490, 625
 Marino, A. F., Villanova, S., Milone, A. P., Piotto, G., Lind, K., Geisler, D., & Stetson, P. B. 2011, *ApJ*, 730, L16
 Marino, A. F., et al. 2014, *MNRAS*, 437, 1609
 Milone, A. P., et al. 2012, *ApJ*, 754, L34
 Milone, A. P., et al. 2014, *MNRAS*, 439, 1588
 Monelli, M., et al. 2015, *ApJ*, 812, 25
 Neeley, J. R., et al. 2015, *ApJ*, 808, 11
 Peimbert, M., Luridiana, V., & Peimbert, A. 2007, *ApJ*, 666, 636
 Pietrinferni, A., Cassisi, S., Salaris, M., & Castelli, F. 2004, *ApJ*, 612, 168
 Pietrinferni, A., Cassisi, S., Salaris, M., & Castelli, F. 2006, *ApJ*, 642, 797
 Pietrzynski, G., et al. 2013, *Nature*, 495, 76
 Pulone, L., de Marchi, G., Paresce, F. 1999, *A&A*, 342, 440
 Pulone, L., Salaris, M., Weiss, A., & Buonanno, R. 1998, *A&A*, 336, 77
 Richer, H.B., et al. 2008, *AJ*, 135, 2141
 Salaris, M., Chieffi, A., & Straniero, A. 1993, *ApJ*, 414, 580
 Salaris, M., & Weiss, A. 1998, *A&A*, 335, 943
 Sarajedini, A., Dotter, A., & Kirkpatrick, A. 2009, *ApJ*, 698, 1872
 Saumon, D., Bergeron, P., Lunine, J. I., Hubbard, W. B., & Burrows, A. 1994, *ApJ*, 424, 333
 Saumon, D., & Marley, M. S. 2008, *ApJ*, 689, 1327
 Schlegel, D. J., Finkbeiner, D. P., & Davis, M. 1998, *ApJ*, 500, 525
 Spergel, D., et al. 2003, *ApJS*, 148, 175
 Stetson, P. B. 1987, *PASP*, 99, 191
 Stetson, P. B. 1994, *PASP*, 106, 250
 Valle, G., Dell'Omodarme, M., Prada Moroni, P. G., Degl'Innocenti, S. 2013, *A&A*, 549, 50
 Valle, G., Dell'Omodarme, M., Prada Moroni, P. G., Degl'Innocenti, S. 2013, *A&A*, 554, 68

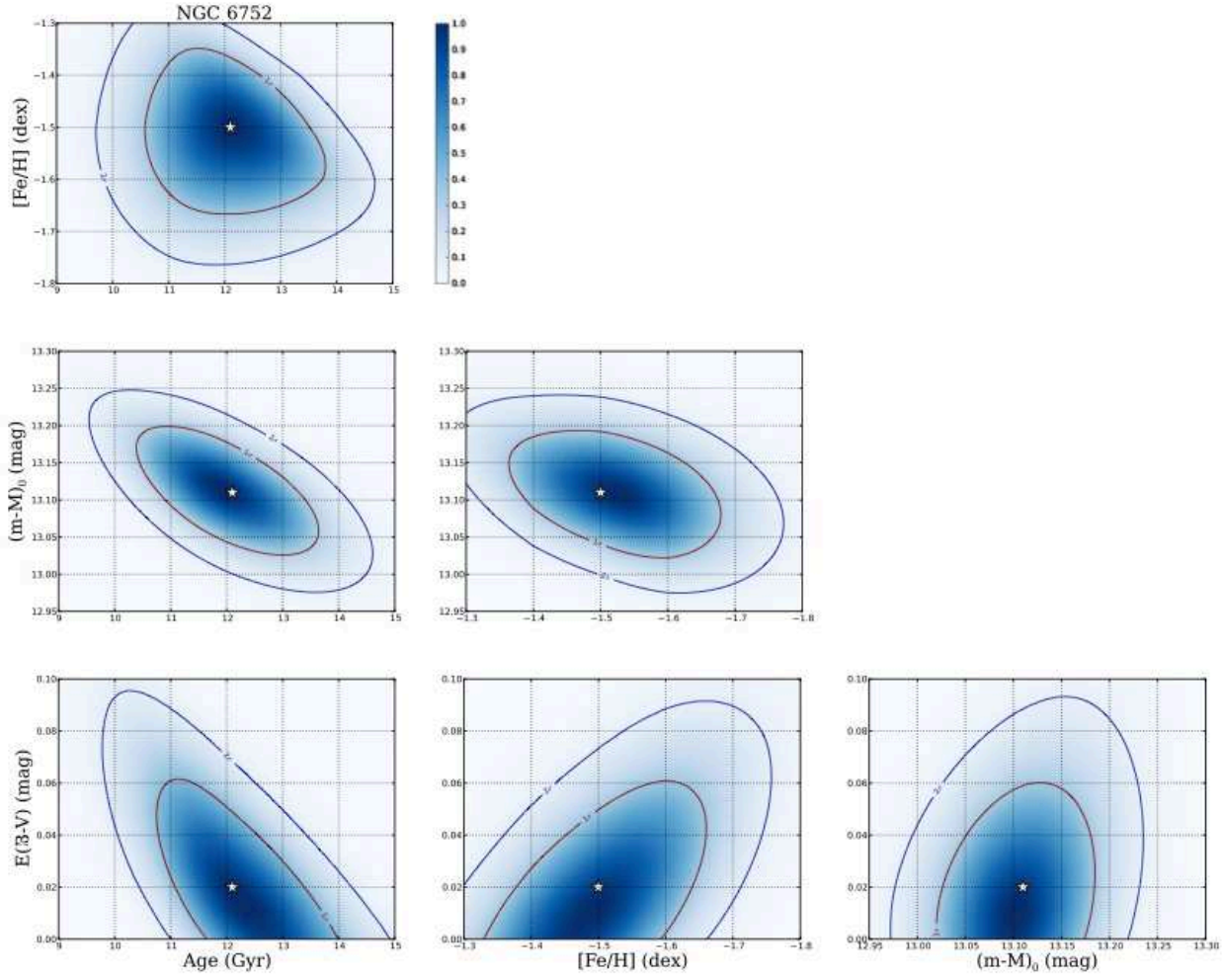


Figure 10. Same as Fig. 7, for the GC NGC 6752

VandenBerg, D. A., Edvardsson, B., Eriksson, K., & Gustafsson, B. 2008, ApJ, 675, 746
 VandenBerg, D. A., et al. 2012, ApJ, 755, 15
 VandenBerg, D. A., Bergbusch, P. A., Ferguson, J. W., & Edvardsson, B. 2014, ApJ, 794, 72
 VandenBerg, D. A., Brogaard, K., Leaman, R., & Casagrande, L. 2013, ApJ, 775, 134

Villanova, S., Geisler, D., Piotto, G., & Gratton, R. G. 2012, ApJ, 748, 62
 Zoccali, M., Cassisi, S., Frogel, J. A., Gould, A., Ortolani, S., Renzini, A., Rich, R. M., & Stephens, A. W. 2000, ApJ, 530, 418

APPENDIX
FIDUCIAL LINE TABLES

In the following table, we report the colors (F110W - F160W), magnitudes (F160W) and errors for the fiducial lines of each GC.

Table 4 Fiducial lines for the four GCs

47 Tuc			M4			NGC 2808			NGC 6752		
F110W - F160W	F160W	σ	F110W - F160W	F160W	σ	F110W - F160W	F160W	σ	F110W - F160W	F160W	σ
0.5915	14.1755	0.0089	0.6265	13.4576	0.0031	0.7744	16.0513	0.0111	0.4769	14.4001	0.0037
0.5905	14.2255	0.0096	0.6241	13.5076	0.0041	0.5858	16.1513	0.0047	0.4775	14.4501	0.0027
0.5776	14.2755	0.0067	0.6118	13.5576	0.012	0.5858	16.2013	0.0053	0.4772	14.5001	0.0035
0.575	14.3256	0.0056	0.604	13.6076	0.002	0.6954	16.2513	0.0204	0.4741	14.5501	0.0052
0.5723	14.3756	0.0046	0.5984	13.6576	0.0034	0.5831	16.3513	0.005	0.4716	14.6001	0.005
0.5711	14.4256	0.0037	0.5907	13.7076	0.0024	0.5799	16.4013	0.005	0.469	14.6501	0.0052
0.5706	14.4756	0.0033	0.5852	13.7576	0.0024	0.5777	16.4513	0.0052	0.4674	14.7001	0.0059
0.5694	14.5256	0.003	0.5796	13.8076	0.0024	0.6041	16.5013	0.0094	0.4647	14.7501	0.0063
0.568	14.5756	0.0028	0.5744	13.8576	0.0024	0.5726	16.5513	0.0054	0.463	14.8001	0.0058
0.5663	14.6256	0.0027	0.5696	13.9076	0.0031	0.5713	16.6013	0.0048	0.4601	14.8501	0.0054
0.5643	14.6756	0.0027	0.565	13.9576	0.0034	0.5684	16.6513	0.0047	0.456	14.9001	0.0047
0.5625	14.7256	0.0029	0.5606	14.0076	0.0035	0.5653	16.7013	0.0046	0.4513	14.9501	0.0043
0.5611	14.7756	0.0032	0.5564	14.0576	0.0032	0.5622	16.7513	0.0045	0.4454	15.0001	0.0041
0.5594	14.8256	0.0033	0.553	14.1076	0.0027	0.5603	16.8013	0.0043	0.4392	15.0501	0.0042
0.5572	14.8756	0.0031	0.55	14.1576	0.0023	0.5573	16.8513	0.0039	0.4322	15.1001	0.0044
0.5542	14.9256	0.0031	0.5477	14.2076	0.0017	0.554	16.9013	0.0036	0.4251	15.1501	0.0047
0.5509	14.9756	0.003	0.5457	14.2576	0.0015	0.5496	16.9513	0.0035	0.4174	15.2001	0.005
0.5479	15.0256	0.0029	0.5438	14.3076	0.0012	0.5441	17.0013	0.0034	0.4098	15.2501	0.0049
0.5458	15.0756	0.0028	0.5421	14.3576	0.0011	0.5364	17.0513	0.0038	0.4028	15.3001	0.0048
0.5429	15.1256	0.0026	0.5406	14.4076	0.001	0.5262	17.1013	0.0039	0.3965	15.3501	0.0046
0.5394	15.1756	0.0027	0.5393	14.4576	0.001	0.5158	17.1513	0.0038	0.3917	15.4001	0.0052
0.5346	15.2256	0.0028	0.5386	14.5076	0.001	0.5057	17.2013	0.0034	0.3876	15.4501	0.0055
0.5278	15.2756	0.0034	0.5383	14.5576	0.0012	0.4968	17.2513	0.0035	0.3848	15.5001	0.0058
0.5207	15.3256	0.0035	0.5388	14.6076	0.0014	0.4897	17.3013	0.0036	0.3819	15.5501	0.0053
0.5137	15.3756	0.0032	0.5394	14.6576	0.0016	0.4826	17.3513	0.0034	0.3798	15.6001	0.0044
0.5048	15.4256	0.0029	0.5403	14.7076	0.0017	0.4763	17.4013	0.0031	0.3774	15.6501	0.0033
0.495	15.4756	0.0036	0.5409	14.7576	0.0017	0.4717	17.4513	0.0026	0.3754	15.7001	0.0026
0.4845	15.5256	0.0039	0.5418	14.8076	0.0017	0.4676	17.5013	0.0024	0.373	15.7501	0.0024
0.4725	15.5756	0.0037	0.5426	14.8576	0.0014	0.4635	17.5513	0.0024	0.3705	15.8001	0.0028
0.4612	15.6256	0.0034	0.5437	14.9076	0.0013	0.4589	17.6013	0.0028	0.3681	15.8501	0.0032
0.4523	15.6756	0.0033	0.5453	14.9576	0.0012	0.4536	17.6513	0.0028	0.3656	15.9001	0.0036
0.4436	15.7256	0.0029	0.5472	15.0076	0.0011	0.4486	17.7013	0.0023	0.3636	15.9501	0.0037
0.436	15.7756	0.0025	0.5493	15.0576	0.0011	0.4447	17.7513	0.0023	0.3619	16.0001	0.0036
0.4304	15.8256	0.0023	0.5515	15.1076	0.0011	0.4416	17.8013	0.0023	0.3609	16.0501	0.0034
0.4252	15.8756	0.0017	0.554	15.1576	0.0014	0.4392	17.8513	0.0024	0.3606	16.1001	0.0031
0.4206	15.9256	0.0015	0.5563	15.2076	0.0012	0.4374	17.9013	0.0021	0.3608	16.1501	0.003
0.4169	15.9756	0.0017	0.5592	15.2576	0.0016	0.4369	17.9513	0.0018	0.3611	16.2001	0.003
0.4131	16.0256	0.0015	0.5621	15.3076	0.0014	0.4369	18.0013	0.0016	0.3623	16.2501	0.0032
0.4095	16.0756	0.0015	0.5657	15.3576	0.0015	0.4371	18.0513	0.0017	0.3634	16.3001	0.0034
0.4067	16.1256	0.0015	0.5692	15.4076	0.0013	0.4372	18.1013	0.002	0.365	16.3501	0.004
0.4048	16.1756	0.0017	0.5732	15.4576	0.0013	0.4373	18.1513	0.0025	0.3676	16.4001	0.0046
0.4038	16.2256	0.0018	0.5776	15.5076	0.0013	0.4376	18.2013	0.0029	0.3697	16.4501	0.0052
0.4039	16.2756	0.0019	0.5826	15.5576	0.0013	0.4385	18.2513	0.003	0.3723	16.5001	0.0056
0.4043	16.3256	0.0019	0.5884	15.6076	0.0015	0.4401	18.3013	0.0027	0.3746	16.5501	0.0059
0.4053	16.3756	0.002	0.595	15.6576	0.0015	0.4424	18.3513	0.0025	0.3775	16.6001	0.0054
0.4065	16.4256	0.002	0.6024	15.7076	0.0016	0.4446	18.4013	0.0024	0.3803	16.6501	0.0055
0.4083	16.4755	0.0018	0.6105	15.7576	0.0016	0.4461	18.4513	0.0022	0.3842	16.7001	0.0053
0.4106	16.5255	0.0018	0.6193	15.8076	0.0017	0.4468	18.5013	0.0022	0.3878	16.75	0.0048
0.4126	16.5755	0.0018	0.6284	15.8576	0.0018	0.4475	18.5513	0.0019	0.3914	16.8	0.0038
0.4145	16.6255	0.0014	0.6387	15.9076	0.002	0.4486	18.6013	0.002	0.3947	16.85	0.0034
0.4165	16.6755	0.0013	0.6493	15.9576	0.002	0.4503	18.6513	0.0023	0.3968	16.9	0.0024
0.4185	16.7255	0.0016	0.6612	16.0076	0.0024	0.4524	18.7013	0.0025	0.3996	16.95	0.0024
0.4217	16.7755	0.0018	0.673	16.0576	0.0024	0.4555	18.7513	0.0026	0.4027	17.0	0.0022
0.4256	16.8255	0.0019	0.6857	16.1076	0.0025	0.459	18.8013	0.003	0.4065	17.05	0.0027
0.4293	16.8755	0.0018	0.6985	16.1576	0.0023	0.4628	18.8513	0.0029	0.4114	17.1	0.0033
0.4333	16.9255	0.0015	0.7117	16.2076	0.0023	0.4671	18.9013	0.0023	0.4164	17.15	0.0036
0.4378	16.9755	0.0016	0.7255	16.2576	0.0024	0.4708	18.9513	0.0022	0.4209	17.2	0.0046
0.4426	17.0255	0.0021	0.7391	16.3076	0.0023	0.4745	19.0013	0.0018	0.4257	17.25	0.0048
0.4486	17.0755	0.0022	0.7532	16.3576	0.0024	0.4785	19.0513	0.0018	0.4292	17.3	0.0054
0.4558	17.1255	0.0025	0.7669	16.4076	0.0023	0.4822	19.1013	0.0017	0.4337	17.35	0.0056
0.463	17.1755	0.0027	0.7805	16.4576	0.0024	0.4858	19.1513	0.0018	0.4374	17.4	0.0059
0.471	17.2255	0.0026	0.7931	16.5076	0.0022	0.4896	19.2013	0.0019	0.4436	17.45	0.0054
0.4796	17.2755	0.0029	0.8048	16.5576	0.0021	0.4939	19.2513	0.0024	0.4493	17.5	0.0048
0.4874	17.3255	0.0028	0.8153	16.6076	0.0018	0.4994	19.3013	0.0026	0.4577	17.55	0.0048
0.495	17.3755	0.0023	0.8241	16.6576	0.0017	0.5063	19.3513	0.0026	0.4657	17.6	0.0046
0.5037	17.4255	0.0027	0.8314	16.7076	0.0014	0.5137	19.4013	0.0027	0.475	17.65	0.0052

Continued on next page

Continued from previous page

47 Tuc			M 4			NGC 2808			NGC 6752		
0.5119	17.4755	0.0032	0.837	16.7576	0.0014	0.5212	19.4513	0.0028	0.4837	17.7	0.0052
0.5213	17.5255	0.0031	0.8418	16.8076	0.0013	0.5296	19.5013	0.0028	0.494	17.75	0.0055
0.5326	17.5755	0.0034	0.8454	16.8576	0.0013	0.5383	19.5513	0.0031	0.5034	17.8	0.0052
0.5437	17.6255	0.004	0.8485	16.9076	0.0011	0.5477	19.6013	0.0032	0.5152	17.85	0.0055
0.5553	17.6755	0.0036	0.8509	16.9576	0.0011	0.5581	19.6513	0.0034	0.5266	17.9	0.0049
0.5694	17.7255	0.0044	0.8527	17.0076	0.001	0.569	19.7013	0.0035	0.5393	17.95	0.0054
0.5838	17.7755	0.0048	0.8538	17.0576	0.0009	0.5794	19.7513	0.0036	0.5506	18.0	0.0052
0.5976	17.8255	0.0048	0.8542	17.1076	0.0009	0.5911	19.8013	0.0036	0.5628	18.05	0.0051
0.6135	17.8755	0.0049	0.8538	17.1576	0.001	0.6025	19.8513	0.0037	0.5732	18.1	0.0052
0.6288	17.9255	0.0049	0.8527	17.2076	0.0012	0.6134	19.9013	0.0041	0.5852	18.15	0.0054
0.6422	17.9755	0.0044	0.8508	17.2576	0.0013	0.6257	19.9513	0.0039	0.5961	18.2	0.0052
0.6557	18.0255	0.0039	0.8484	17.3076	0.0016	0.6388	20.0013	0.0043	0.6085	18.25	0.0053
0.6688	18.0755	0.004	0.8458	17.3576	0.0018	0.6512	20.0513	0.0044	0.6203	18.3	0.0055
0.6804	18.1255	0.004	0.8431	17.4076	0.002	0.6635	20.1013	0.0041	0.6323	18.35	0.0055
0.6912	18.1755	0.0038	0.8408	17.4576	0.002	0.6759	20.1513	0.004	0.6432	18.4	0.0053
0.7025	18.2255	0.0035	0.8387	17.5076	0.002	0.6868	20.2013	0.0041	0.6518	18.45	0.0048
0.712	18.2755	0.0037	0.837	17.5576	0.0019	0.6978	20.2513	0.0043	0.6589	18.5	0.0041
0.7204	18.3255	0.0031	0.8356	17.6076	0.0017	0.7087	20.3013	0.0043	0.6624	18.55	0.0034
0.7286	18.3755	0.0026	0.8343	17.6576	0.0017	0.7188	20.3513	0.0037	0.6655	18.6	0.0033
0.7344	18.4255	0.0023	0.8332	17.7076	0.0017	0.7278	20.4013	0.0031	0.6666	18.65	0.0032
0.7385	18.4755	0.0018	0.8322	17.7576	0.0021	0.7361	20.4513	0.003	0.6678	18.7	0.0036
0.7416	18.5255	0.0017	0.8314	17.8076	0.0023	0.7431	20.5013	0.0028	0.6688	18.75	0.0036
0.7432	18.5755	0.0018	0.8306	17.8576	0.0025	0.7488	20.5513	0.0026	0.6694	18.8	0.0039
0.7441	18.6255	0.0019	0.8299	17.9076	0.0023	0.7534	20.6013	0.0024	0.6696	18.85	0.0037
0.7444	18.6755	0.0019	0.8288	17.9576	0.0023	0.7565	20.6513	0.0022	0.6691	18.9	0.0041
0.7444	18.7255	0.002	0.8276	18.0076	0.0019	0.7583	20.7013	0.0024	0.6685	18.95	0.0038
0.7434	18.7755	0.002	0.8264	18.0576	0.0019	0.76	20.7513	0.0027	0.6666	19.0	0.0044
0.7416	18.8255	0.002	0.8255	18.1076	0.0016	0.76	20.8013	0.0029	0.6668	19.05	0.0049
0.739	18.8755	0.0021	0.8247	18.1576	0.002	0.7598	20.8513	0.0033	0.6657	19.1	0.006
0.7364	18.9255	0.0025	0.8241	18.2076	0.0024	0.7593	20.9013	0.0039	0.6666	19.15	0.0061
0.7334	18.9755	0.0025	0.8221	18.2576	0.0033	0.7576	20.9513	0.004	0.6658	19.2	0.0066
0.7309	19.0255	0.0027	0.8203	18.3076	0.0039	0.756	21.0013	0.0046	0.6661	19.25	0.0052
0.7283	19.0755	0.0025	0.8166	18.3576	0.0049	0.7534	21.0513	0.0042	0.6648	19.3	0.0052
0.7254	19.1255	0.0025	0.8141	18.4076	0.0048	0.7521	21.1013	0.0045	0.6636	19.35	0.0048
0.7229	19.1755	0.0023	0.811	18.4576	0.0044	0.7514	21.1513	0.0052	0.663	19.4	0.0052
0.7201	19.2255	0.0024	0.8095	18.5076	0.0041	0.7486	21.2013	0.0045	0.6627	19.45	0.0057
0.7177	19.2755	0.0025	0.8075	18.5576	0.0044	0.7474	21.2513	0.0042	0.6626	19.5	0.0067
0.7148	19.3255	0.003	0.8065	18.6076	0.0053	0.7462	21.3013	0.004	0.6614	19.55	0.0078
0.7119	19.3755	0.003	0.8046	18.6576	0.0062	0.7438	21.3513	0.0032	0.6592	19.6	0.0096
0.7088	19.4255	0.0031	0.8032	18.7076	0.0072	0.7422	21.4013	0.0033	0.656	19.65	0.0106
0.7055	19.4755	0.003	0.8021	18.7576	0.0072	0.7398	21.4513	0.0031	0.6539	19.7	0.0106
0.7022	19.5255	0.0036	0.8019	18.8076	0.007	0.7376	21.5013	0.003	0.6525	19.75	0.0107
0.6989	19.5755	0.0036	0.8035	18.8576	0.0068	0.7363	21.5513	0.0026	0.6517	19.8	0.0113
0.6956	19.6255	0.0043	0.8057	18.9076	0.0062	0.735	21.6013	0.0029	0.6512	19.85	0.0137
0.6917	19.6755	0.0042	0.8074	18.9576	0.0056	0.7335	21.6513	0.0031	0.6499	19.9	0.0156
0.6881	19.7255	0.0045	0.8095	19.0076	0.0045	0.7321	21.7013	0.0036	0.6485	19.95	0.0176
0.685	19.7755	0.0041	0.8101	19.0576	0.004	0.731	21.7513	0.0032	0.647	20.0	0.018
0.6821	19.8255	0.0045	0.8099	19.1076	0.005	0.7305	21.8013	0.0034	0.6473	20.05	0.0184
0.6804	19.8755	0.0049	0.8108	19.1576	0.0051	0.7303	21.8513	0.0036	0.6495	20.1	0.0173
0.6792	19.9255	0.0065				0.7295	21.9013	0.0041	0.6533	20.15	0.0158
0.6766	19.9755	0.0066				0.7291	21.9513	0.0035	0.6559	20.2	0.0144
0.6743	20.0255	0.0072				0.7281	22.0013	0.0036	0.658	20.25	0.0132
0.6705	20.0755	0.0069				0.7268	22.0513	0.0036	0.6579	20.3	0.0153
0.6675	20.1255	0.0067				0.7258	22.1013	0.0048	0.6525	20.35	0.0143
0.6642	20.1755	0.0072				0.7275	22.1513	0.0048	0.6577	20.4	0.0328
0.6623	20.2255	0.0089				0.7271	22.2013	0.0062	0.6301	20.45	0.0098
0.6593	20.2755	0.0106				0.7266	22.2512	0.0075	0.628	20.5	0.007
0.6588	20.3255	0.0116				0.7263	22.3012	0.0068			
0.6555	20.3755	0.0092				0.7285	22.3512	0.0097			
0.6547	20.4255	0.0082				0.7298	22.4012	0.0109			
0.6513	20.4755	0.0081				0.7317	22.4512	0.0128			
0.6507	20.5255	0.0083				0.7313	22.5012	0.0122			
0.6481	20.5755	0.0083				0.7348	22.5512	0.0139			
0.6464	20.6255	0.0077				0.7356	22.6012	0.0122			
0.6439	20.6755	0.0066				0.7373	22.6512	0.0127			
0.6419	20.7255	0.0063				0.7358	22.7012	0.0122			
0.6394	20.7755	0.0061				0.7386	22.7512	0.011			
0.6383	20.8255	0.0063				0.738	22.8012	0.0125			
0.6357	20.8755	0.0064				0.737	22.8512	0.0137			
0.6338	20.9255	0.0056				0.7346	22.9012	0.0121			
0.6318	20.9755	0.0052				0.7399	22.9512	0.0124			
0.631	21.0255	0.0048				0.7347	23.0012	0.0148			
0.6283	21.0755	0.0049				0.7284	23.0512	0.0146			
0.6276	21.1255	0.0053				0.7265	23.1012	0.0102			
0.6256	21.1755	0.0056				0.7352	23.2012	0.0129			
0.6245	21.2255	0.0055				0.7157	23.2512	0.0086			
0.623	21.2755	0.0046				0.7133	23.3012	0.0072			
0.6214	21.3255	0.0047				0.7133	23.3512	0.01			

Continued on next page

Continued from previous page

47 Tuc			M 4	NGC 2808			NGC 6752
0.6197	21.3755	0.0044		0.7602	23.4012	0.0288	
0.6183	21.4255	0.0048		0.733	23.4512	0.0397	
0.6177	21.4755	0.005					
0.6162	21.5255	0.0051					
0.6158	21.5755	0.0052					
0.6143	21.6255	0.0051					
0.6169	21.6755	0.0089					
0.6158	21.7255	0.0116					
0.6241	21.7755	0.0219					
0.6276	21.8255	0.0273					
0.6365	21.8755	0.0293					
0.6437	21.9255	0.0264					
0.6656	21.9755	0.0147					
0.6428	22.0255	0.036					
0.6926	22.0755	0.0427					